S Lazerson et al.

First measurements of error fields on W7-X using flux surface mapping

First measurements of error fields on W7-X using flux surface mapping ‡

Samuel A. Lazerson[1]**, Matthias Otte**[2]**, Sergey Bozhenkov**[2]**, Christoph Biedermann**[2]**, Thomas Sunn Pedersen**[2] **and the W7-X Team**[2]

[1]Princeton Plasma Physics Laboratory, Princeton NJ, 08543, USA
[2]Max-Planck-Institut für Plasmaphysik, 17491, Greifswald, Germany

E-mail: lazerson@pppl.gov

Abstract. Error fields have been detected and measured using the flux surface mapping diagnostic system on Wendelstein 7-X (W7-X). A low-field '$\iota = 1/2$' magnetic configuration ($\iota = \iota/2\pi$), sensitive to error fields, was developed in order to detect their presence using the flux surface mapping diagnostic. In this configuration, a vacuum flux surface with rotational transform of $n/m = 1/2$ is created at the mid-radius of the configuration. If no error fields are present a small $n/m = 5/10$ island chain should be present. Modeling indicates that if an $n = 1$ perturbing field is applied by the trim coils, a large $n/m = 1/2$ island chain will be opened. This island chain is used to create a perturbation large enough to be imaged by the diagnostic. Phase and amplitude scans of the applied field allow the measurement of a small $\sim 0.04\ m$ intrinsic island chain with a 140° phase relative to the first module of the W7-X experiment. These error fields are determined to be small and easily correctable by the trim coil system.

PACS numbers: 52.70.Ds,52.55.Hc

Submitted to: *Nuclear Fusion*

1. Introduction

The W7-X experiment has been designed to achieve high plasma performance through careful optimization of both the magnetic geometry and topology [1, 2]. Thus the assessment and compensation of magnetic fields which are detrimental to the experiment plays a key role in achieving high performance. In particular, it has been shown that error fields with toroidal mode number $n = 1$ can overload divertor targets at relatively modest levels of (relative) error field amplitude. Such fields can arise from a variety of sources including coil assembly [3], ferritic materials, and superconducting coil motion [4]. To compensate such fields, five water cooled copper trim coils have been installed outside the cryostat of the device [5, 6]. These coils serve a dual purpose as they can be used to both compensate error field effects and introduce an error field in a controlled manner. Figure 1 depicts the location of the trim coils relative to plasma of W7-X, along with the flux surface mapping diagnostic. In this work, the trim coils were used to create a large magnetic island which could be directly imaged via the flux surface mapping diagnostic in W7-X. This provides us with the first measurement of error fields in the W7-X experiment.

Flux surface measurement is a capability unique to stellarators and heliotrons, due to the presence of flux surfaces in vacuum [7, 8, 9]. This diagnostic technique uses a beam of electrons to trace out the magnetic field lines of the device. This is possible because, in vacuum, the electrons will stay tied to the magnetic field lines on which they start. If a trace amount of background gas is puffed into the vacuum vessel a light trace is generated, which can then be imaged by a camera. This is due to the inelastic collisional excitation of the gas by the electron beam. Alternatively, a fluorescent screen or swept rod may be used to image a flux surface, producing a Poincaré-like plot. This second method relies on the electron beam making many passes through the device. On each pass, the beam causes the rod or screen to fluoresce. In W7-X a hybrid rod-emitter system is used [10]. In this system, two fluorescent rods (a third is prepared for installation after the initial operation phase) with electron emitters are installed on the machine, allowing one rod to serve as the emitter while the other sweeps across the electron beam while being imaged by a camera. What makes this diagnostic technique even more interesting is that it require no plasma. Thus it avoids complications added by interpreting signals in terms of plasma response models. Moreover, it can be preformed before a stellarator or heliotron is fully operational, providing insights into the device before plasma operation begins.

A new magnetic configuration, the '$\iota = 1/2$', was developed so that flux surface mapping could begin to provide information about the intrinsic error fields of W7-X. In this configuration, a flux surface with rotational transform ($\iota = n/m$) of $1/2$ is present halfway between the magnetic axis and inboard limiter (figure 2). If no error fields were present, such a configuration is expected to have a vanishingly small $n/m = 5/10$ island chain present at this surface. The presence of error fields (intrinsic or applied by the trim coils) will open an island chain at this surface. In the following
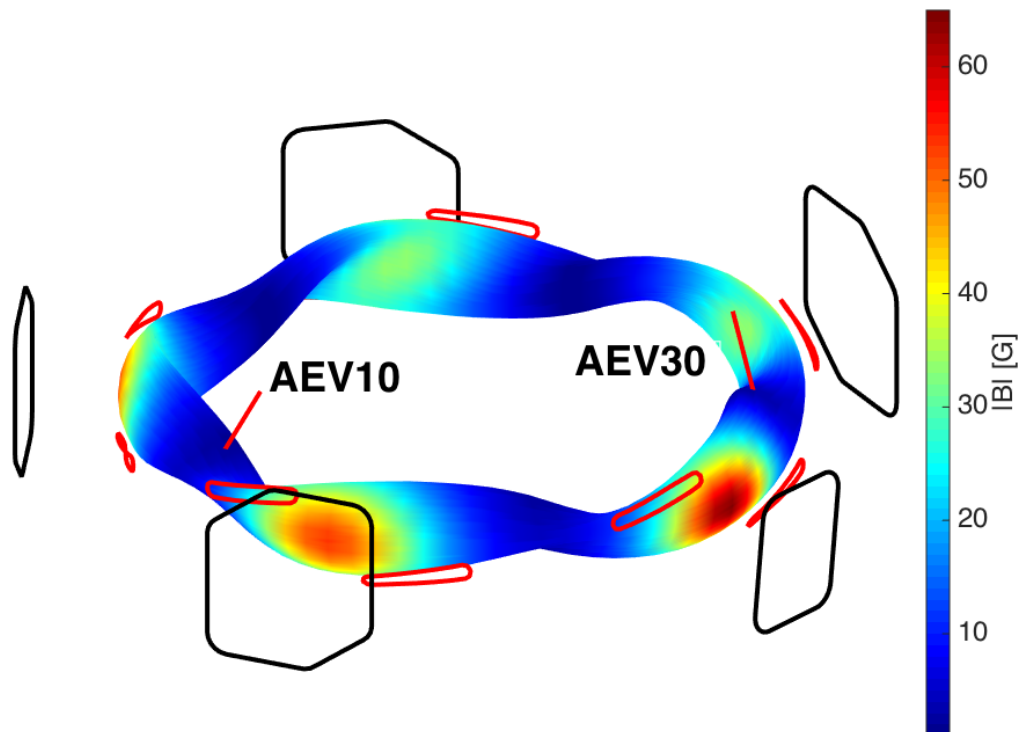
Figure 1. The trim (black) and sweep coils (red) are depicted against an edge flux surface of W7-X. Color contours indicate intensity of normal field created by each trim coil (1000 A). The centerline of the AEV10 and AEV30 ports, where the flux surface mapping manipulators are located, are depicted by red lines.

sections, measurements are presented investigating this magnetic configuration in W7-X. In the next section, the diagnostic configuration and development of a synthetic flux surface mapping diagnostic are described. In section 3, the diagnostic measurements are presented for various applied trim coil fields. In section 4, estimates are made of the error fields in W7-X from the flux surface measurements. Finally, in section 5 the results are summarized and their implications on plasma operations are discussed.

2. Methods

In this work, simulations informed the development of the '$\iota = 1/2$' configuration so that flux surface measurements could be made which probed the error field of W7-X. The simulation work involved field line tracing in vacuum fields and the development of a synthetic diagnostic for flux surface mapping. Development of the synthetic diagnostic directly tied the simulations to the geometric realities of the experiment. With the configuration established, experiments involving the application of trim coil fields could be conducted.

W7-X Rotational Transform Comparision
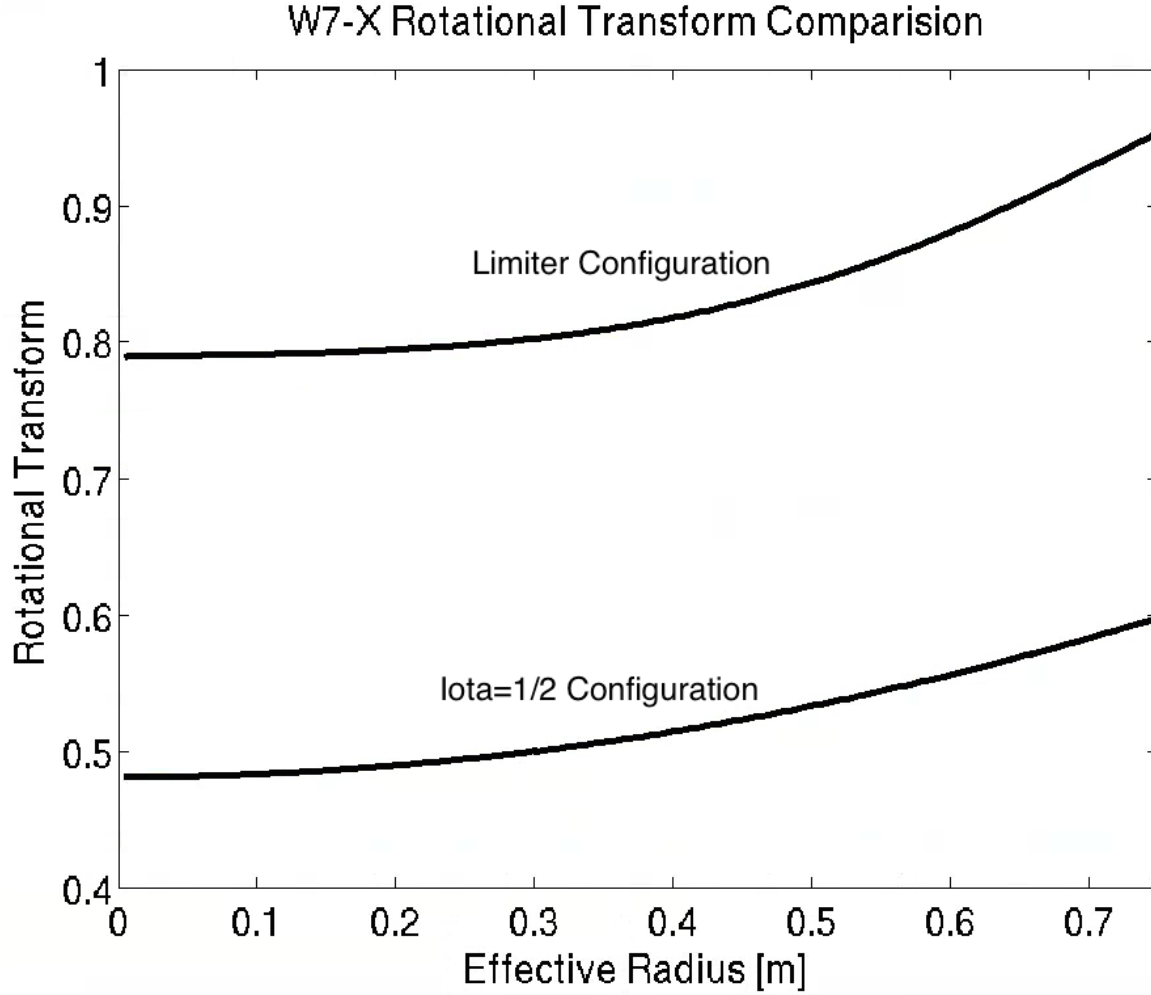
Figure 2. Rotational transform of the newly developed $\iota = 1/2$ configuration as compared to the limiter configuration envisioned for plasma operation in the first operational phase. Note the reduced edge magnetic shear in the new configuration.

To simulate the trajectories of magnetic field lines in vacuum, the FIELDLINES code was developed in parallel with a second web-based service for W7-X [11]. The equation of motion for a particle tracing out a magnetic field line is rather simple

$$\frac{\partial \vec{x}}{\partial t} = \vec{B} \tag{1}$$

where $\vec{x}$ is position, t time, and $\vec{B}$ the magnetic field. This may be rewritten in cylindrical coordinates to eliminate the time dependence from the equations

$$\frac{\partial R}{\partial \phi} = \frac{B_R}{B_\phi} \tag{2}$$

$$\frac{\partial Z}{\partial \phi} = \frac{B_Z}{B_\phi} \tag{3}$$

where R, Z, and ϕ are the cylindrical radial, vertical and toridal coordinates respectively. Thus tracing the trajectory of a field line becomes the task of solving a rather trivial set

of ordinary differential equations (ODEs). It is important to note that these equations will trace out field lines which lay on flux surfaces along with those which lay in magnetic islands or stochastic regions. The FIELDLINES code constructs cubic hermite polonomial splines [12] of the magnetic field using an accurate Biot-Savart integration method [13]. Integration of the ODEs is performed using one of three methods (advanced Adams [14], LSODE [15], or Runge-Kutta [16]). The code also contains diagnostic routines for finding periodic orbits [17]. These routines are used for magnetic axis location, X-point location, and to trace out the unstable (stable) manifolds associated with periodic orbits.

While tracing individual field lines provides a useful tool it can often times be difficult to compare to flux surface measurements. In figure 3, a Poincaré trace using the FIELDLINES code is compared to flux surface mapping conducted in the WEGA stellarator [8]. While both appear qualitatively similar, details in the Poincaré plot do not appear in the flux surface mapping image. Additionally, features present in the experimental image are hard to discern in the Poincaré plot. Such difficulties motivated the development of a synthetic diagnostic capable of mimicking the experimental setup.

In order to develop such a synthetic diagnostic, the unique geometry of the actual diagnostic in W7-X must be taken into account as well. This includes the location of the emitter, location (and orientation) of the plane swept by the fluorescent rod, and the view parameters of the camera itself. Poincaré traces are started from the actual emitter location as defined by the port structure, manipulator insertion length, and rod angle. The rod itself does not sweep in a constant toroidal plane (Figure 4), unlike most Poincaré tracing codes which assume constant toroidal cuts (ϕ constant). To accommodate this geometry a 'transparent' wall surface was implemented
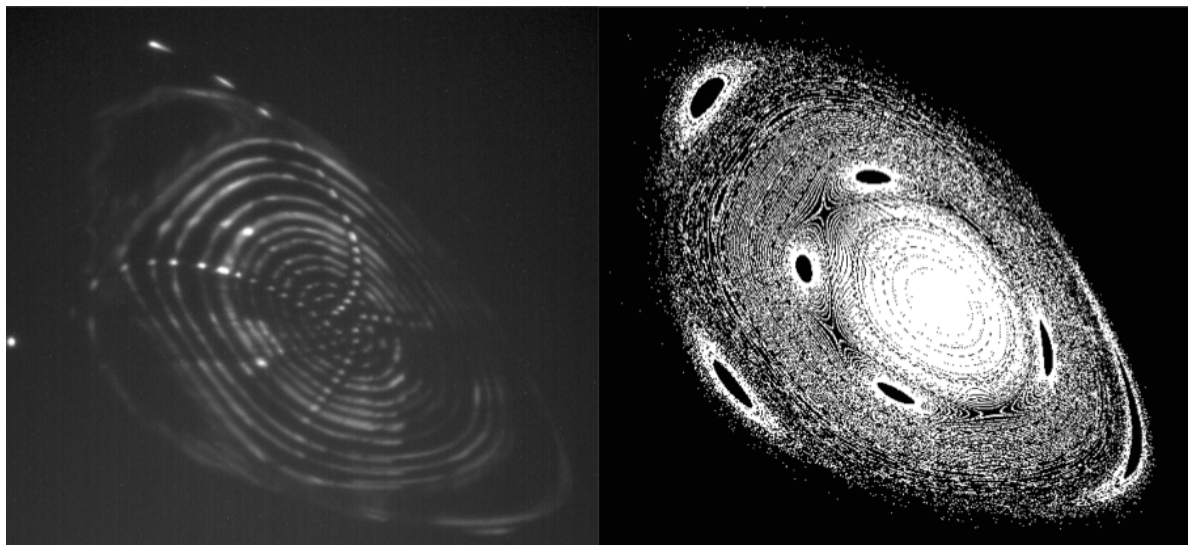

Figure 3. Comparison between flux surface mapping image (left) and vacuum Poincaré plot (right) for the WEGA stellarator. Significantly more detailed information is present in the Poincaré plot making comparisons qualitative.
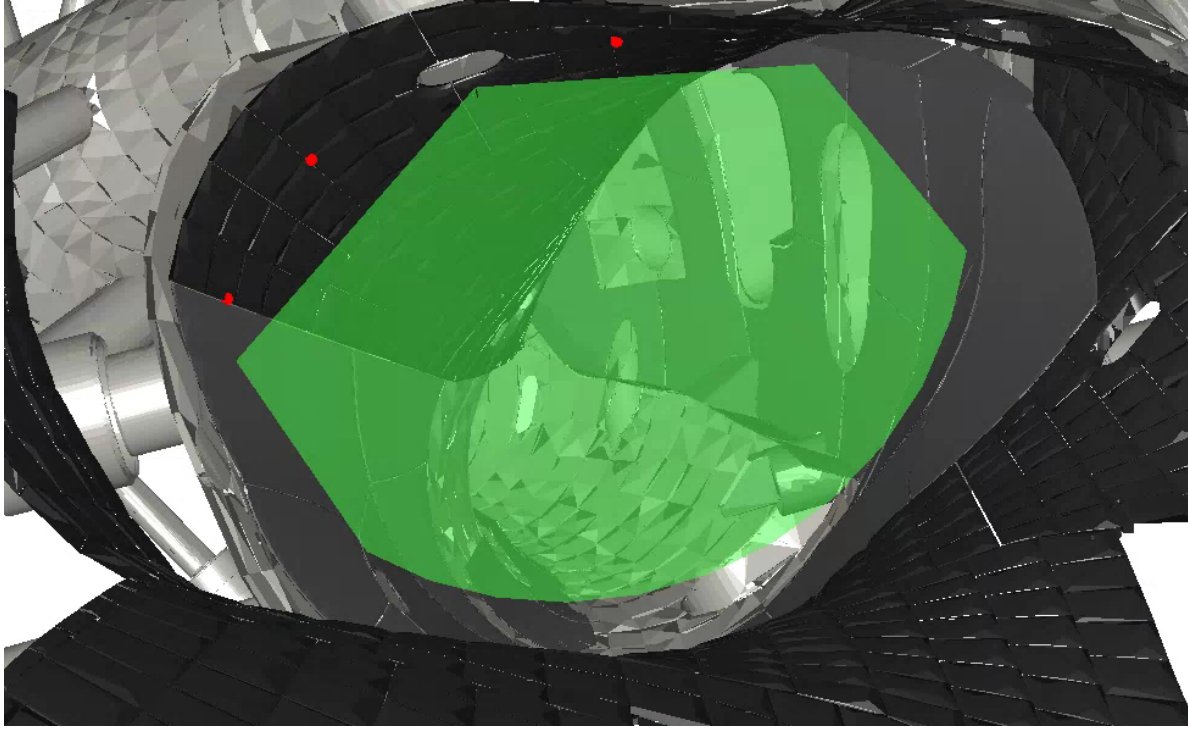
Figure 4. Depiction of the measurement plane swept out by the flourescent rod in port AEV30 (green). The plane is inclined with respect to the vertical and horizontal directions, implying that a constant phi plane approximation would not be accurate. Red dots indicate the location of the alignment light fibers. Some of the W7-X vessel, first wall and port structures have been plotted for reference.

in the FIELDLINES code. This surface records where a particle strikes but continues the integration of the particle trajectory (unlike a real wall which would stop the integration). The wall model itself is defined as a tessellated triangular mesh allowing it to describe arbitrary surface shapes. In this case, the rod traces out a rather simple plane. In order to generate an accurate image of these points, the camera itself must be modeled as well. For this task a simple pinhole camera model was assumed. In order to calibrate spatial location of the camera, four light fibers were installed in the carbon wall tiles. The locations of the fibers were measured to a high degree of accuracy after installation. Using these positions a synthetic image of the fibers can be compared against measured data. The simulated camera position, rotation, pointing direction, and focal length can then be modified to provide a best fit to the measured location of the light fibers. Such fitting showed that the camera in the AEQ21 port was rotated by 14.5957^o, had a focal length of 16.1095 mm, was located 10.1735 mm behind the port flange, and was misaligned to the port normal vector by 2.3703^o (figure 5 looking at the detection plane of the manipulator in AEV30 in module 3). These values are consistent with the estimated parameters of the installation. Such information allows each pixel of the camera to be mapped to real space co-ordinates as defined by the manipulator geometry.
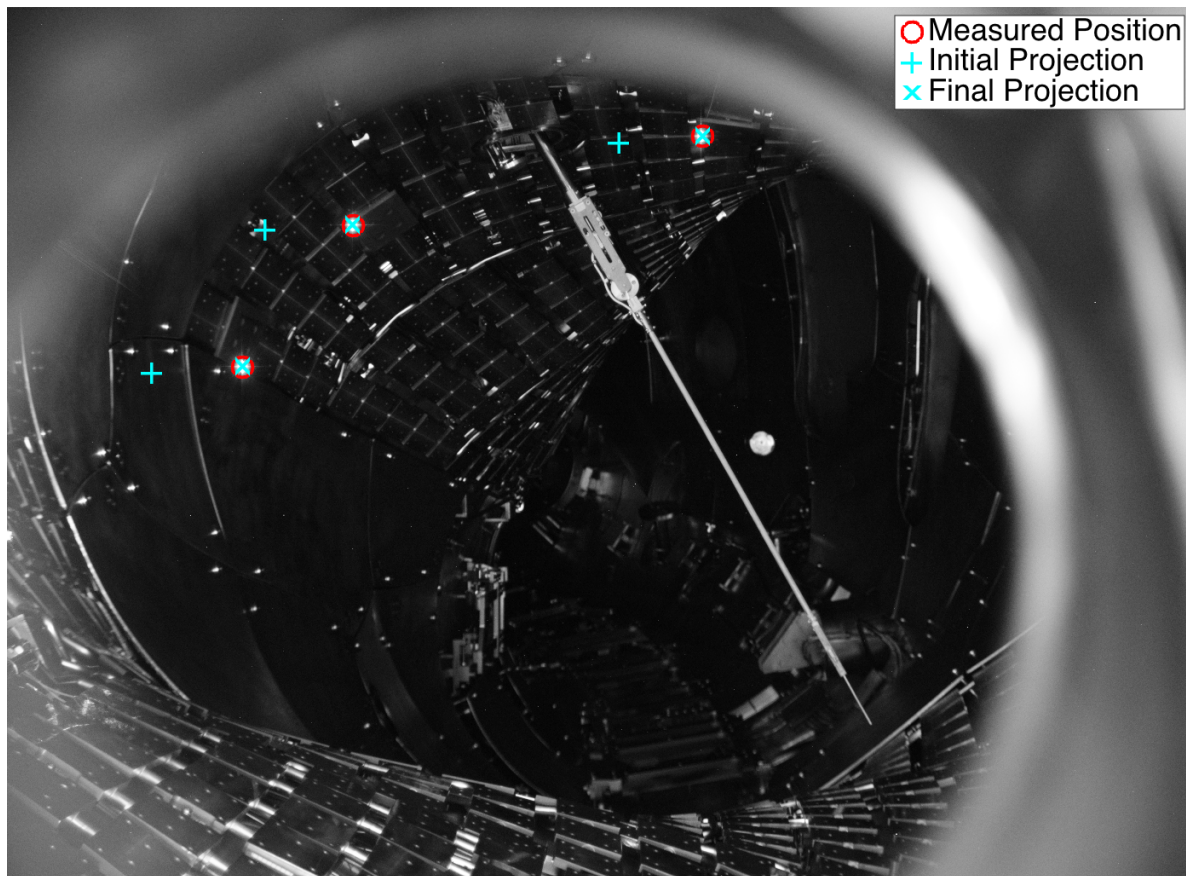
Figure 5. Figure showing the optimization of the synthetic diagnostic viewing angle, rotation, and normal vector for the camera in port AEQ21. Red circles indicate the pixel location of the light fibers as measured by the actual diagnostic. Optimized position matches measured values within a pixel.

Table 1. Coil currents in the non-planar coils (NPC1-5) and planar coils (PCA-B) for the $\iota = 1/2$ configuration. All currents in A per turn. NPC coils have 108 turns and PC have 36 turns.

NPC1	NPC2	NPC3	NPC4	NPC5	PCA	PCB
510	1030	2050	3070	4100	5000	5000

Measurement of error fields using this diagnostic required that a configuration be developed which responds to the presence of such fields. The majority of pre-defined coil current configurations in W7-X avoid flux surfaces with low order rational rotational transform in the bulk plasma. This is accomplished through a combination of low shear and careful configuration choice. The experiment itself was designed to be robust to the effects of error fields. To measure the error fields, a special configuration was developed with an $\iota = 1/2$ surface present at the mid radius of the vacuum flux surfaces. This was achieved by lowering the currents in non-planar coils while fixing the current in the planar coils at $5\ kA$ (Table 1). This results in a much lower field ($\sim 0.3\ T$) than found
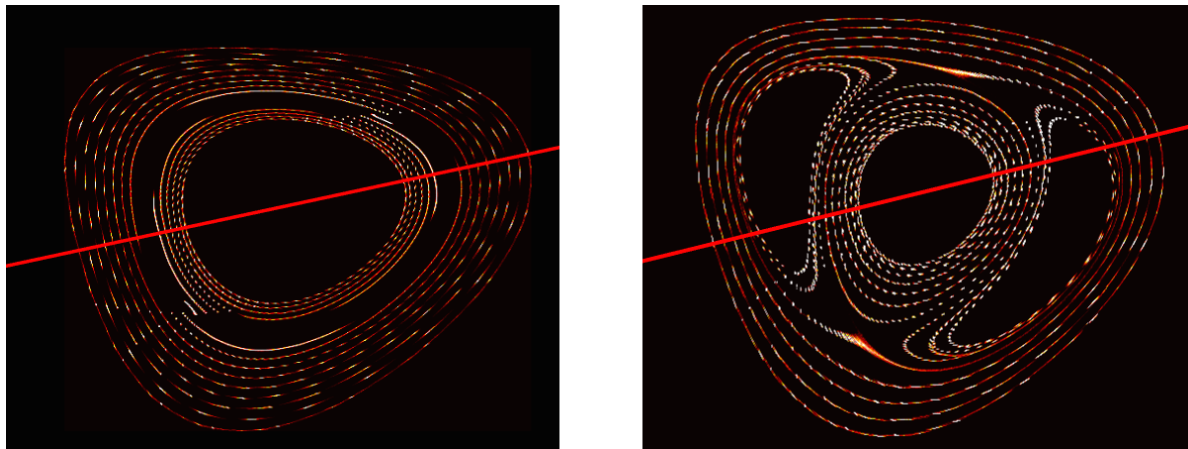
Figure 6. Synthetic diagnostic image of $\iota = 1/2$ configuration without applied error fields (left) and with an applied $n = 1$ error field from the trim coils (right). Synthetic diagnostic emitter stepped with 0.02 m increments, in the port axial direction. The solid red line indicates the $z = 0$ plane, which is tilted with respect to the camera sensor.

during plasma operation ($\sim 2.5\ T$). While not feasible for plasma operation, such a low field is acceptable for flux surface mapping. Additionally, care was taken to vary the non-planar coil currents to achieve two goals. The first being to increase the shear of the configuration, thus minimizing emitter self-shadowing of the electron beam after two passes ($m = 2$, $n = 1$ field line pitch). The second being to move the configuration farther from the limiter structure. The resulting configuration contained only a small $n/m = 5/10$ island chain when evaluated using the ideal coil set, but allowed a large $n/m = 1/2$ island chain to be opened by application of the trim coils (figure 6). Thus a configuration had been developed which responded to error fields with $n = 1$ character in a unique way (the $m = 2$ island chain).

3. Results

Measurements of the $n = 1$ error field in W7-X were performed using the $\iota = 1/2$ configuration and the flux surface mapping diagnostic. An initial attempt was made to image any island chain which may arise from an intrinsic error field. This failed to resolve any surfaces near the $\iota = 1/2$ resonance due to emitter self-shadowing. Mappings of the flux surfaces with the trim coils energized in an $n = 1$ pattern were then performed. Island width scaling with applied trim coil field was investigated along with the phase of the applied field. For all finite amplitudes and phases an, $m = 2$, $n = 1$ island chain was clearly resolved. These experiments provided a wealth of data for analysis.

Attempts to directly image an island chain due to intrinsic error fields proved difficult due to self-shadowing of the emitter arm. Figure 7 is a composite image of many emitter positions scanning radially outward. The line of bright dots indicates the first and second passes of the emitter beam. Flux surfaces in the inner radial regions
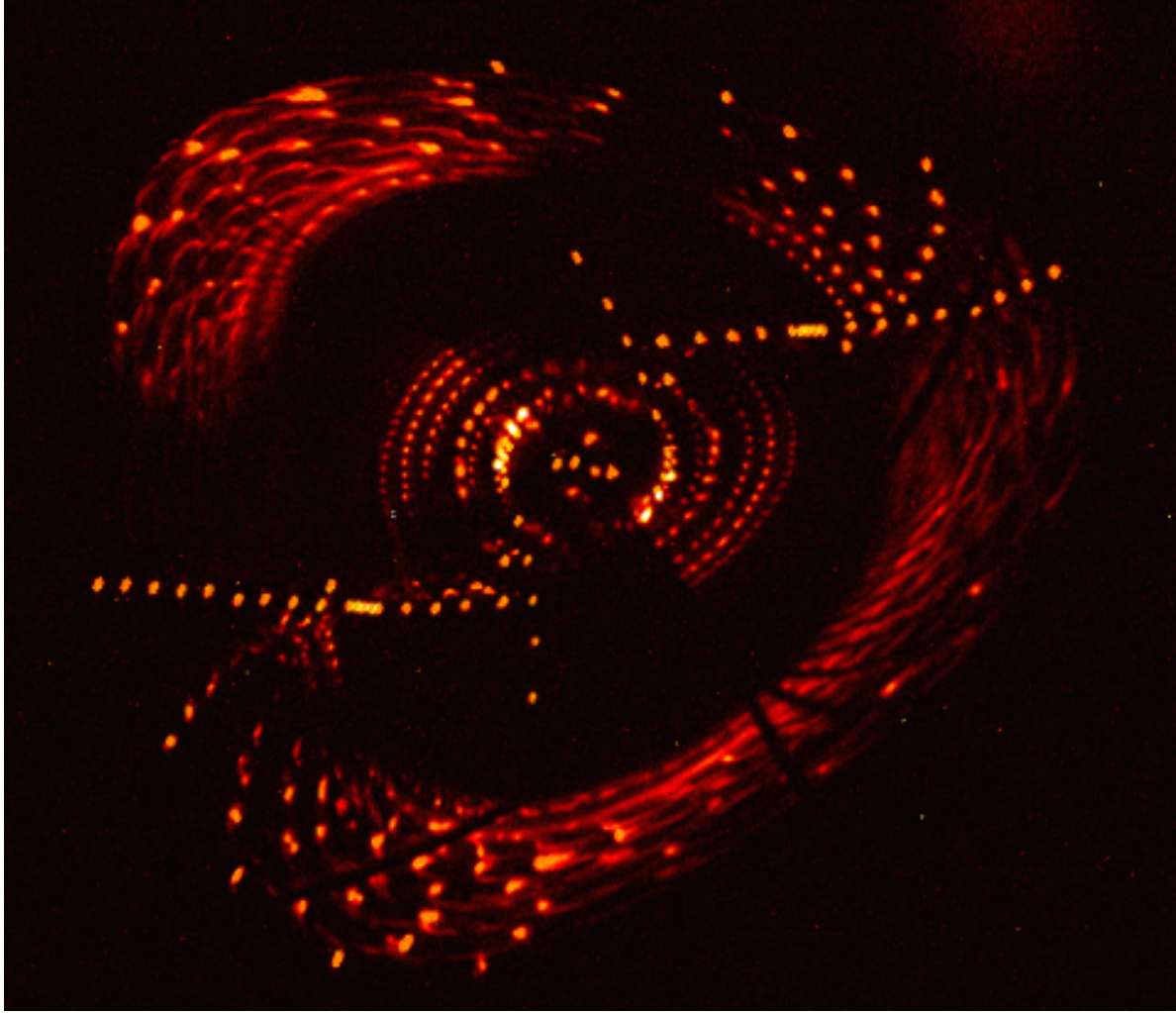
Figure 7. Composite flux surface mapping diagnostic image showing the $\iota = 1/2$ configuration with no applied trim coil fields (false color). Inner flux surfaces are clearly visible although shadowing prevents half of the surfaces from being imaged. The dark annular region is due to the emitter self-shadowing near the $\iota = 1/2$ surface. The radial lines of bright dots indicate first and second passes of the emitter beam.

can be clearly seen encircling the magnetic axis of the configuration. These surfaces are missing about half their trace due to shadowing effects. A large dark annular region is present due to self-shadowing of the emitter beam. This prevented a direct imaging of the magnetic topology near the $\iota = 1/2$ surface. Farther outside this region the flux surface traces return but with additional features which are attributed to an interaction of the fluorescent rod and beam itself. However, the self-shadowing effect is still present at higher field levels. The final radial point made only one transit, presumably hitting a limiter structure.

The self-shadowing of the emitter beam is a reality of any configuration, with low shear and near a rational surface. At the $\iota = 1/2$ surface a field line will make two passes around the machine before returning exactly to the position from which the trace was
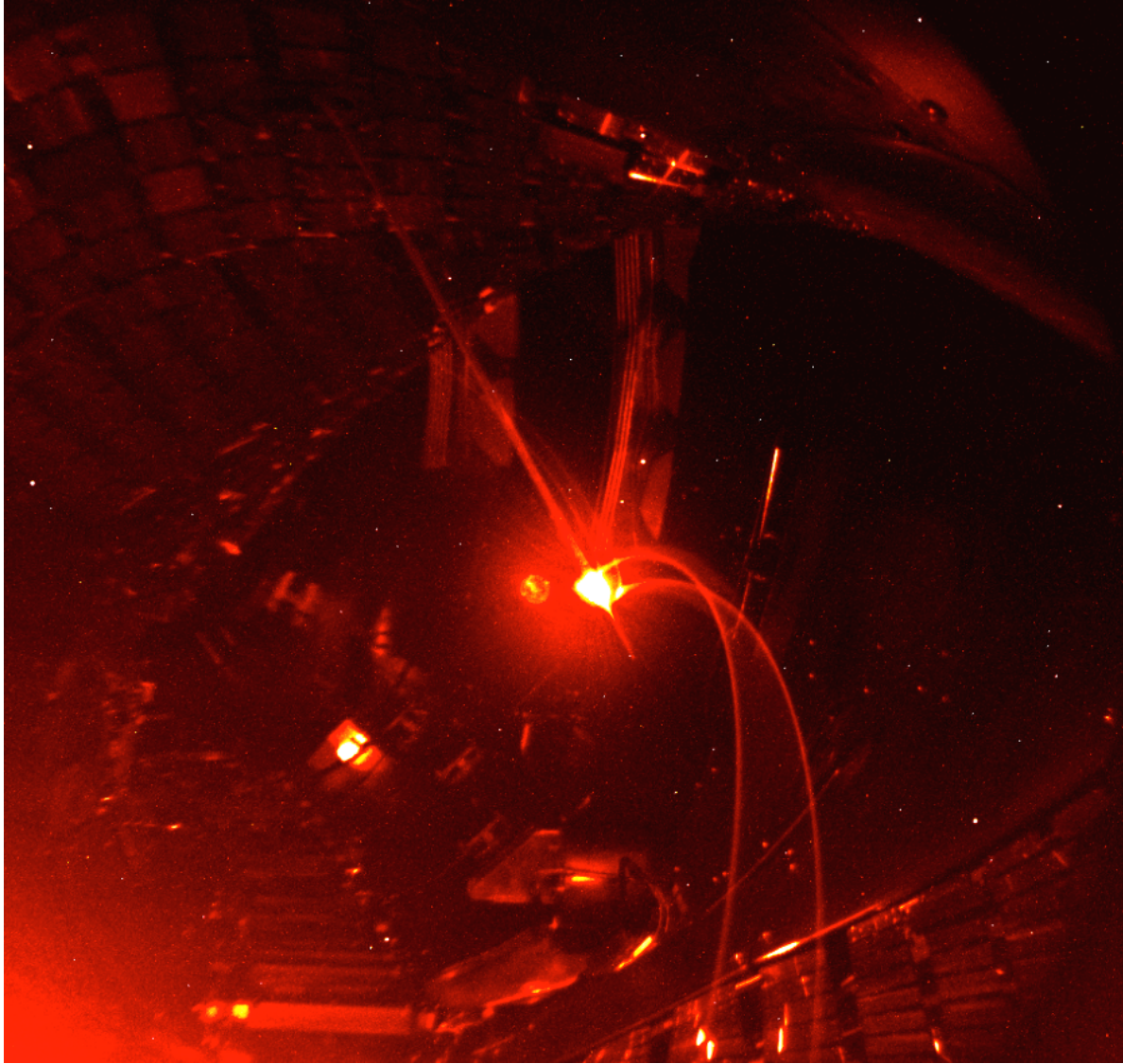
Figure 8. Image from the AEQ51 port viewing the electron beam emitter showing self-shadowing of emitter beam after two passes. Gas was puffed into the vessel to visualise the electron beam. Image is false color.

started. As the emitter moves away from this rational surface the trace just misses the starting position allowing more passes of the field line trajectory. The finite thickness of the emitter rod then translates to a finite annular region around the rational surface wherein the electron beam is in the shadow of the emitter. Figure 8 was taken from the camera sitting in the AEQ51 port, viewing the emitter rod. Argon gas has been puffed into the vessel, allowing the electron beam to be clearly visualized. The beam clearly makes two passes before hitting the back of the emitter beam causing a bright fluorescent spot on the back of the rod.

The presence of the braided looking flux surfaces in the region exterior to the $\iota = 1/2$ surface is attributed to an interaction between the fluorescent rod and the electron beam. Figure 9 compares two visualizations, one in which the rod is swept
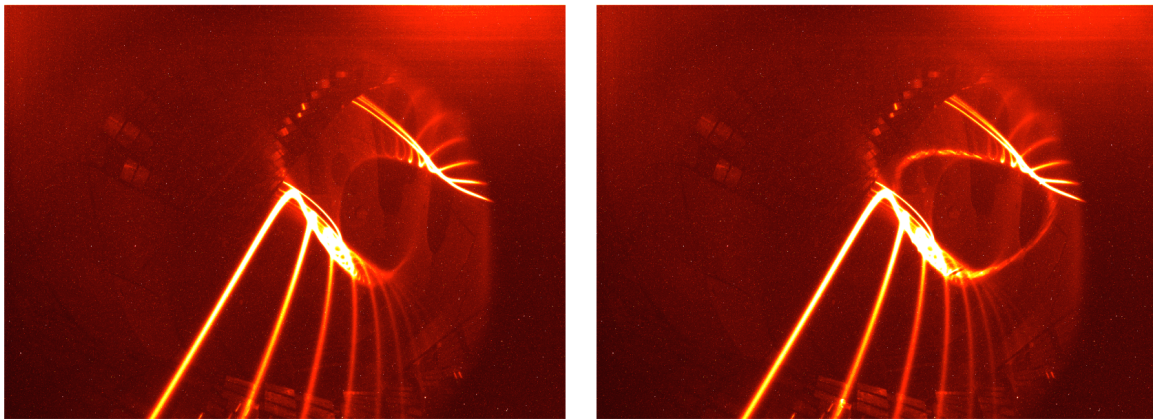
Figure 9. Electron beam visualizations (false color) showing edge flux surface without fluorescent rod sweep (left) and with rod sweep (right). The blurry edge flux surface appears to be due to some interaction of the rod with the electron beam.

and one in which it is not. The image in which the rod is swept indicates the presence of a blurred or braided flux surface, while the image in which the rod is not swept shows no such feature. The fact that the first ~ 20 passes of the beam are clearly visible and regular seem to indicate that this is not a stochastic or ergodic region. The exact nature of these edge features is unknown but may be due to charging of a small insulating ceramic on the swept rod and the associated $\vec{E} \times \vec{B}$ drift of the electrons.

Since the intrinsic island chain could not be imaged, the trim coils were used to open the $n/m = 1/2$ island chain by applying an $n = 1$ waveform at 50, 100, and 200 A peak trim coil current. Figure 10 shows three false-color composite images at each of these trim coil amplitudes. At 50 A current the island is still not directly imaged but small interior flux surface like features are present along with a deformation of the outer flux surface consistent with the presence of an island. The 100 and 200 A cases, clearly resolve the separatrix of an island with $m = 2$ character. In the 200 A case surface interior to the island are partially imaged.
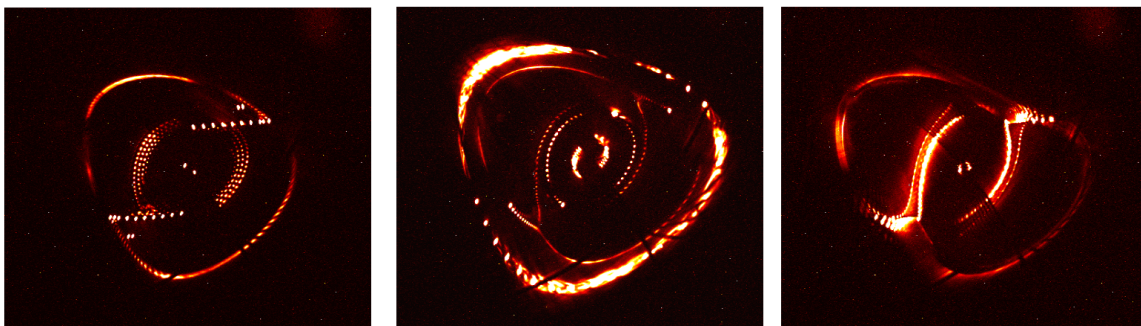
Figure 10. Comparison of images taken at 50 A (left), 100 A (center), and 200 A (right) peak trim coil current with $n = 1$ waveform.
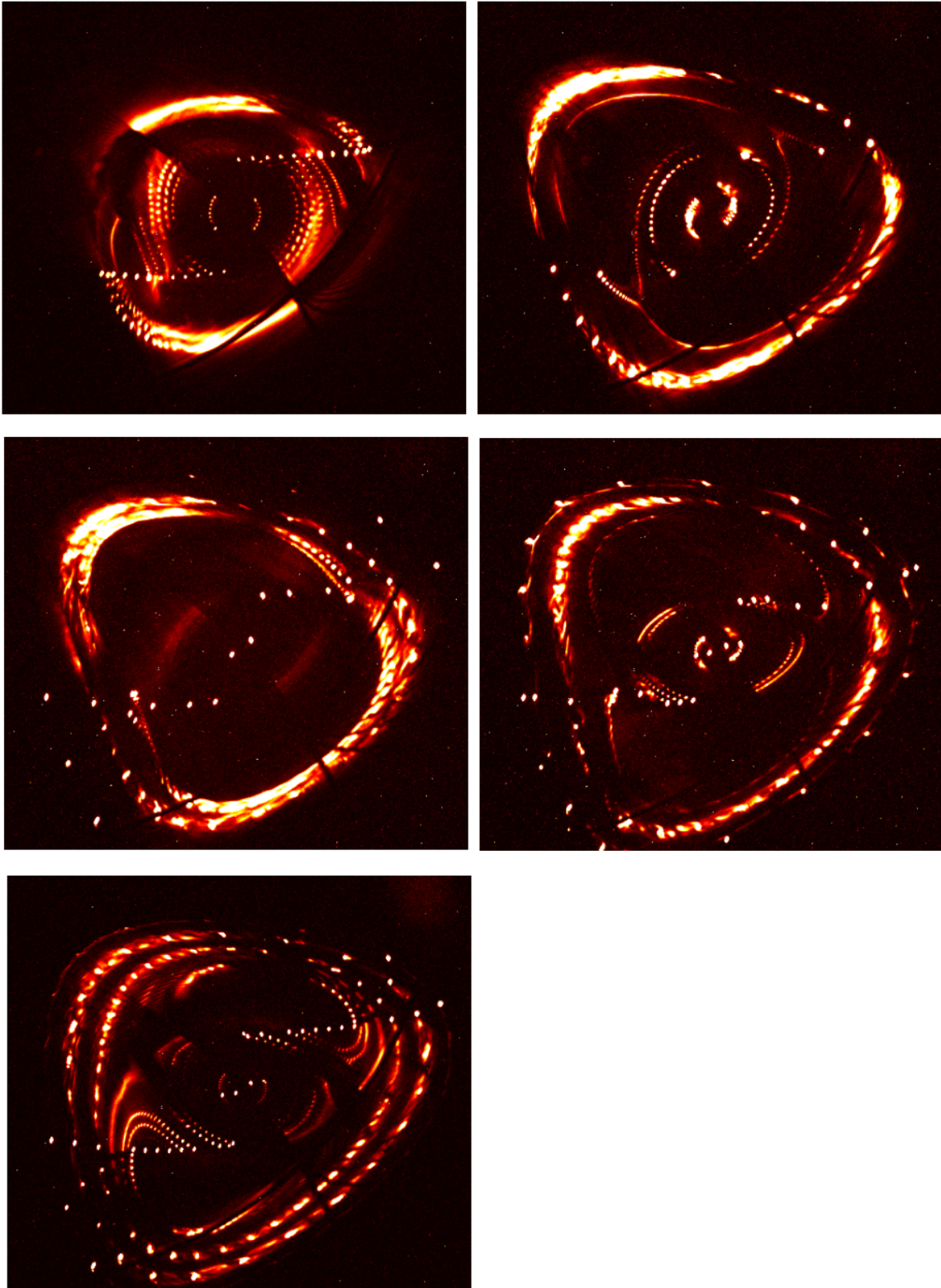
Figure 11. False color images comparing variation in the applied phase of an $n = 1$ trim coil field at fixed amplitude (100 A). Phases are 0° (upper left), 72° (upper right), 144° (middle left), 216^8 (middle right), and 288° (lower left).

A scan of the applied trim coil phase was conducted locking the peak amplitude of the $n = 1$ field to a trim coil at 100 A. Figure 11 compares the composite images from each phase. The island chain clearly rotates as the applied field is rotated, in this context phase is defined in terms of center of the trim coil in module 1 (counterclockwise as view from above is taken to be the positive direction, the positive toroidal magnetic field direction). For 0° phase the islands appear the smallest and are least discernible. The separatrix was clearly visible at the 72° phase. It was for this reason that the amplitude scans were performed at this phase. The 288° phase allowed partial flux surfaces inside the island chain to be imaged. As in the case with no applied trim coil field, the edge surfaces appear to distort due to the electron-beam interaction with the sweeping rod.

4. Analysis

The data from the previous section can be further analyzed to determine the minimum detectable island chain, the width of the intrinsic island chain, and the phase of the intrinsic error field. The minimum detectable island chain is set by the shear of the magnetic configuration and emitter shadowing. We can ask the question how large must an island become for the second pass of the electron beam to miss the emitter. By examining the scaling of the island width with applied trim coil current, the size of the intrinsic island may be determined. The island width dependance on applied trim coil phase allows the phase of the intrinsic error field to be determined.

The minimum detectable island width may be determined by examining how far a field line moves in the plane from which it is launched. In our case, the second full toroidal pass will be of interest, as this is the pass which would fall within the shadow of the emitter rod. For simplicity, we treat the emission plane as being in a constant toroidal plane (a close approximation to the real system). We take the rod to be 12 mm wide (electron gun is 10 mm wide), inclined with respect to the vertical direction in the poloidal plane by 14°, and inclined with respect to the vertical direction in the toroidal direction by 24°. Using these values we can approximate a field line as shadowed if it does not move at least 0.18 m in the vertical direction after two passes. This gives us an annular region which is ~ 0.13 m wide, where only two passes will be recorded. This is in approximate agreement with experimental measures showing a ~ 0.10 m region where flux surface were not detected (see figure 7). A more sophisticated analysis using the synthetic diagnostic is left to future work.

Although an intrinsic island may be too small to be directly visualized, the trim coil amplitude scaling scan can be used to determine the size of the intrinsic island. We note that the island width (in the small width limit) can be predicted by [18]

$$w = \sqrt{\frac{R_0 B_{mn}}{m B_0 \, \iota'}}, \tag{4}$$

where R_0 is the major radius, B_{mn} is the amplitude of the resonant harmonic, m is the poloidal harmonic, B_0 is the total magnetic field strength, and $\iota' = d\iota/d\rho$ is the
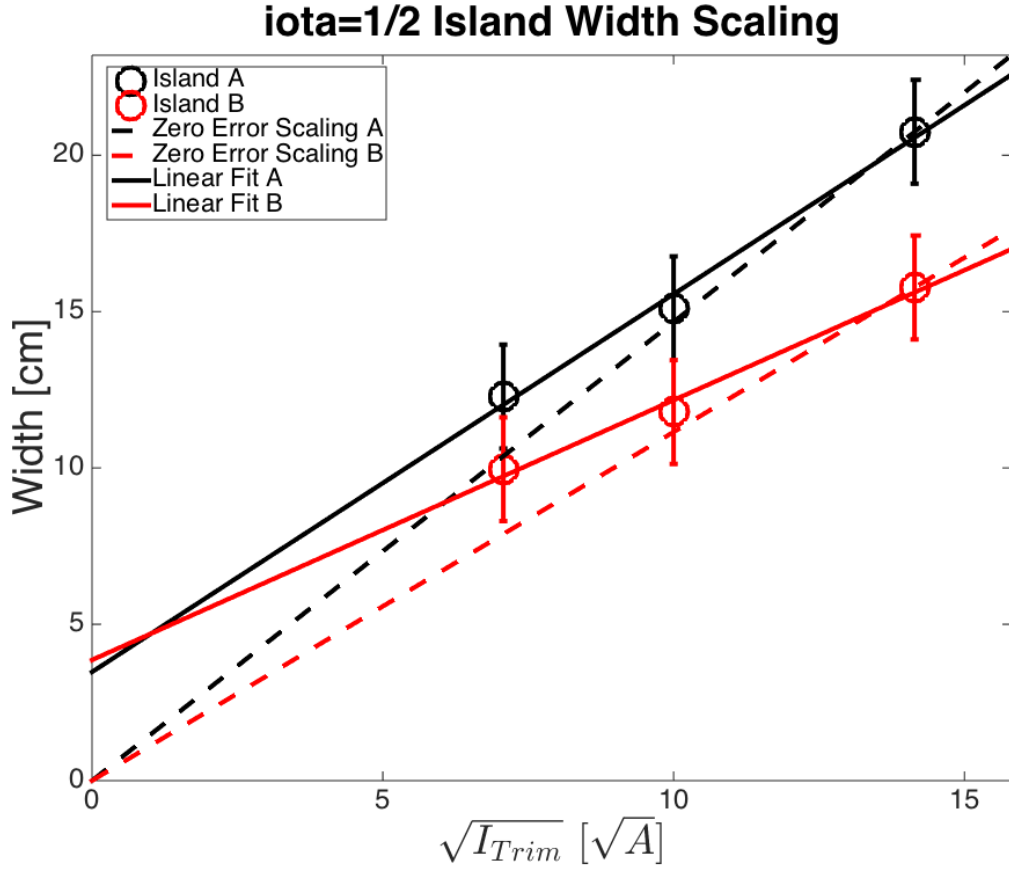
Figure 12. Plot of island widths obtained from flux surface mappings scanning applied trim coil field. Scaling of both lobes of the island suggest a small residual island is present at zero applied trim coil current.

magnetic shear across the rational surface. Here we can equate the resonant harmonic with the amplitude of the applied $n = 1$ trim coil field. This gives us the relation that

$$w \propto \sqrt{I_{trim}}, \tag{5}$$

where I_{trim} is the maximum current in the trim coils. To map the experimental data to real space we use the conversion that 1 pixel is equal to 1/6 cm, a number obtained from the synthetic diagnostic of the camera image. Figure 12 depicts the scaling of island widths due to applied trim coil currents. The scaling suggests that at zero applied trim coil current, the island width should be $\sim 4\ cm$. This would also equate to an island produced by 10 A peak trim coil current. Scaling the low field of the $\iota = 1/2$ configuration to the nominal 2.5 T plasma operation field, we find that the trim coil currents must be scaled as well. This suggests that such an error could be corrected at 2.5 T using only 80 A peak trim coil current, which is $\sim 4\ \%$ the maximum rated peak coil current of 2000 A. It should be noted that this analysis is for the $m = 2$ harmonic, while the $m = 1$ harmonic is predicted to be larger.

Inspection of the trim coil phase scan shows both a dependence of island width and island phase on the applied trim coil phase. As the trim coil fields and error field
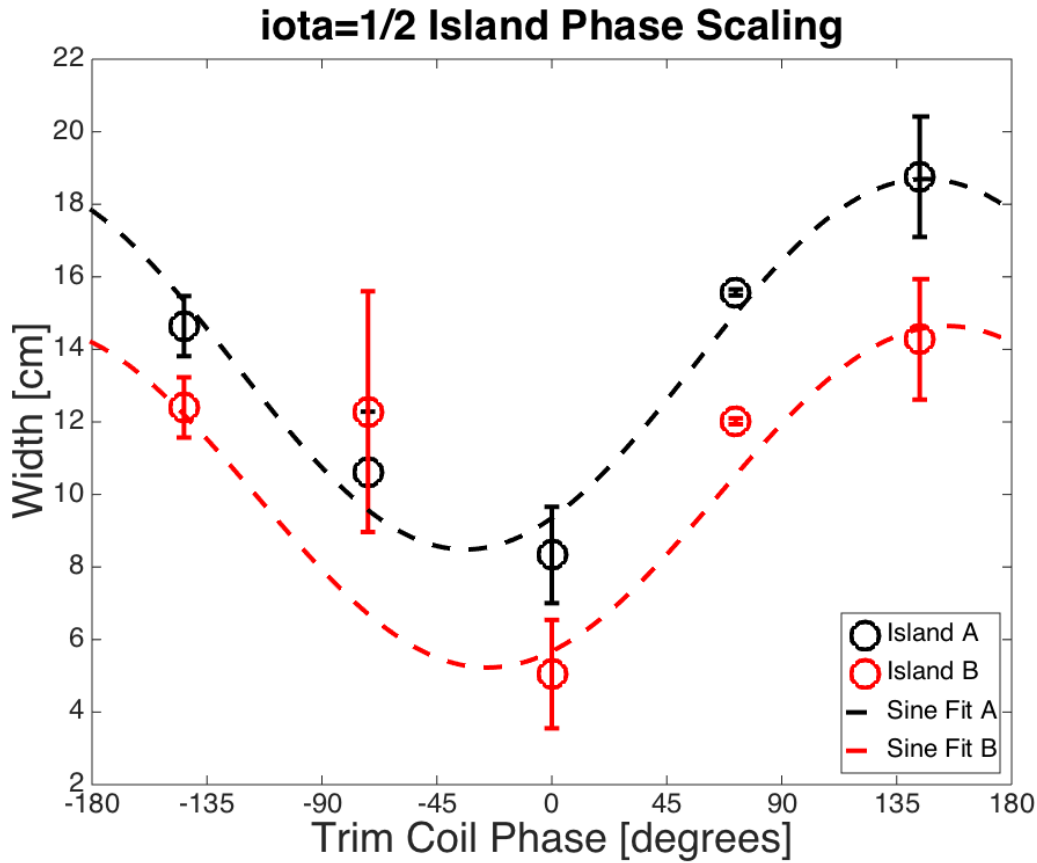
Figure 13. Plot of island widths obtained from flux surface mappings scanning applied trim coil phase at fixed magnetic field. The function $w(\theta) = A * \sin(\theta + B) + C$ was fit to each set of points.

linearly superimpose, it can be expected that the island width would be a minimum when the trim coil phase directly opposes the intrinsic island phase. Similarly, when the phases align the island chain should be large. Figure 13 depicts the island width dependence on applied trim coil phase. Fitting a sine wave to the data points $(w(\theta) = A * \sin(\theta + B) + C)$, a minimum around $\sim -40^o$ is clearly present for both island chains. This is suggestive of an intrinsic error field with a phase of $\sim 140^o$. Only one outlier exists for this dataset, and it's value is attributed to difficulties determining an accurate island width for that image.

5. Discussion

Using a newly developed magnetic configuration, the '$\iota = 1/2$' configuration, the first error fields in W7-X have been detected using the flux surface mapping diagnostic. In these set of experiments, the trim coils were exercised to open a $n/m = 1/2$ island chain which could be clearly imaged. The small intrinsic island chain due to an error field could not be imaged due to electron beam emitter shadowing. However, a scan of trim

coil amplitude using an $n = 1$ waveform revealed the possibility of a ~ 4 *cm* intrinsic island chain. Scans of the phase of the applied $n = 1$ field suggest the error field has a phase of $\sim 140^o$ relative to module 1. Correction of such an error field at 2.5 T would require $\sim 4\%$ of the total available trim coil current.

While the measurement of the $n/m = 1/2$ error field provides insight into the presence of error fields, one may ask if anything about the $n/m = 1/1$ error field can be inferred. If the source of the error field is the same, then measuring one confirms the presence of the other. However, to make a solid statement regarding the $n/m = 1/1$ error field requires additional modeling. Such modeling is left to future work, specifically at a time when the superconducting coil misalignment data has been fully processed. Additionally, experiments are planned to directly assess the $n/m = 1/1$ error field after the first experimental campaign. It should be noted that since these measurements were made at low field, a direct comparison with the as-measured coil positions is possible. At low field, the coils should have minimal electromagnetic force deformation. Modeling of this configuration may provide confirmation of coil positioning. This is valuable because the superconducting coil positions were measured before cool-down and before the vessel baking.

It should also be noted that at the time of these experiments, a large amount of black steel scaffolding was distributed around the torus hall, providing an additional source of error fields. These have since been replaced with aluminium scaffolding. The experiments presented here will be repeated to confirm the effect of the scaffolding.

This exercise also highlights a desirable feature regarding reactor construction, namely the measurement and assessment of error fields before plasma operation. One could envision a stellarator reactor with large perturbing coils placed outside the cryostat (and possibly outside the bio-shield). The error fields could then be measured well in advance of plasma operation. If these coils were relocatable, a more optimized set of correcting coils could be installed on the device. This could ease assembly tolerances, avoid in-vessel coils, and overall reduce the construction cost of the reactor.

Acknowledgments

[1] H S Bosch, R C Wolf, T Andreeva, J Baldzuhn, D Birus, T Bluhm, T Bräuer, H Braune, V Bykov, A Cardella, F Durodié, M Endler, V Erckmann, G Gantenbein, D Hartmann, D Hathiramani, P Heimann, B Heinemann, C Hennig, M Hirsch, D Holtum, J Jagielski, J Jelonnek, W Kasparek, T Klinger, R König, P Kornejew, H Kroiss, J G Krom, G Kühner, H Laqua, H P Laqua, C Lechte, M Lewerentz, J Maier, P McNeely, A Messiaen, G Michel, J Ongena, A Peacock, T S Pedersen,

R Riedl, H Riemann, P Rong, N Rust, J Schacht, F Schauer, R Schroeder, B Schweer, A Spring, A Stäbler, M Thumm, Y Turkin, L Wegener, A Werner, D Zhang, M Zilker, T Akijama, R Alzbutas, E Ascasíbar, M Balden, M Banduch, Ch Baylard, W Behr, Craig D Beidler, A Benndorf, T Bergmann, C Biedermann, B Bieg, W Biel, M Borchardt, G Borowitz, V Borsuk, Sergey A Bozhenkov, R Brakel, H Brand, Thomas Brown, B Brucker, R Burhenn, K P Buscher, C Caldwell-Nichols, A Cappa, A Cardella, A Carls, P Carvalho, ? Ciupiński, M Cole, J Collienne, A Czarnecka, G Czymek, G Dammertz, C P Dhard, V I Davydenko, A Dinklage, M Drevlak, S Drotziger, A Dudek, P Dumortier, G Dundulis, P v Eeten, K Egorov, T Estrada, H Faugel, J Fellinger, Y Feng, H Fernandes, W H Fietz, W Figacz, F Fischer, J Fontdecaba, A Freund, T Funaba, H Fünfgelder, A Galkowski, David A Gates, L Giannone, J M García Regaña, Joachim Geiger, S Geißler, H Greuner, M Grahl, S Groß, A Grosman, H Grote, O Grulke, M Haas, L Haiduk, H-J Hartfuß, J H Harris, D Haus, B Hein, P Heitzenroeder, P Helander, R Heller, C Hidalgo, D Hildebrandt, H Höhnle, A Holtz, E Holzhauer, R Holzthüm, A Huber, H Hunger, F Hurd, M Ihrke, S Illy, A Ivanov, S Jablonski, N Jaksic, M Jakubowski, R Jaspers, H Jensen, H Jenzsch, J Kacmarczyk, T Kaliatk, J Kallmeyer, U Kamionka, R Karaleviciu, S Kern, M Keunecke, R Kleiber, J Knauer, R Koch, G Kocsis, A Könies, M Köppen, R Koslowski, J Koshurinov, A Kramer-Flecken, R Krampitz, Y Kravtsov, M Krychowiak, G Krzesinski, I Ksiazek, Fr Kubkowska, A Kus, S Langish, R Laube, M Laux, Samuel Lazerson, M Lennartz, C Li, R Lietzow, A Lohs, A Lorenz, F Louche, L Lubyako, A Lumsdaine, A Lyssoivan, Henning Maaßberg, P Marek, C Martens, N Marushchenko, M Mayer, B Mendelevitch, Ph Mertens, David R Mikkelsen, A Mishchenko, B Missal, T Mizuuchi, H Modrow, T Mönnich, T Morizaki, S Murakami, F Musielok, M Nagel, D Naujoks, H Neilson, O Neubauer, U Neuner, R Nocentini, J M Noterdaeme, Carolin Nührenberg, S Obermayer, G Offermanns, H Oosterbeek, Matthias Otte, A Panin, M Pap, S Paquay, E Pasch, X Peng, S Petrov, D Pilopp, H Pirsch, B Plaum, F Pompon, M Povilaitis, J Preinhaelter, O Prinz, F Purps, T Rajna, S Récsei, Allan H Reiman, D Reiter, J Remmel, S Renard, V Rhode, J Riemann, S Rimkevicius, K Risse, A Rodatos, I Rodin, M Romé, H J Roscher, K Rummel, Th Rummel, A Runov, L Ryc, J Sachtleben, A Samartsev, M Sanchez, F Sano, A Scarabosio, M Schmid, H Schmitz, O Schmitz, M Schneider, W Schneider, L Scheibl, M Scholz, G Schröder, M Schröder, J Schruff, H Schumacher, I V Shikhovtsev, M Shoji, G Siegl, J Skodzik, M Smirnow, E Speth, D A Spong, R Stadler, Z Sulek, V Szabó, T Szabolics, T Szetefi, Z Szökefalvi-Nagy, A Tereshchenko, H Thomsen, M Thumm, D Timmermann, H Tittes, K Toi, M Tournianski, U v Toussaint, J Tretter, S Tulipán, P Turba, R Uhlemann, J Urban, E Urbonavicius, P Urlings, S Valet, D Van Eester, M Van Schoor, M Vervier, H Viebke, R Vilbrandt, M Vrancken, T Wauters, M Weissgerber, and E... Weiß. Technical challenges in the construction of the steady-state stellarator Wendelstein 7-X. *Nuclear Fusion*, 53(12):126001, November 2013.

[2] Joachim Geiger, Craig D Beidler, Y Feng, Henning Maaßberg, N B Marushchenko, and Y Turkin. Physics in the magnetic configuration space of W7-X. *Plasma Physics and Controlled Fusion*, pages 1–11, November 2014.

[3] T Andreeva, T Bräuer, M Endler, J Kisslinger, and Yu Igitkhanov. Analysis of the magnetic field perturbations during the assembly of wendelstein 7-x. *Fusion science and technology*, 46(2):388–394, 2004.

[4] N Jaksic, P van Eten, V Bykov, and F Schauer. Analysis of the magnet support structure for the plasma fusion experiment wendelstein 7-x. *Comp. and Struct.*, 89:1177–1191, 2011.

[5] Thomas Rummel, Konrad Risze, Frank Fullenbach, Matthias Koppen, Johann Kisslinger, Tom Brown, Ron Hatcher, Stephen Langish, Mike Mardenfeld, and George Hutch Neilson. The Wendelstein 7-X Trim Coil System. *IEEE Transactions on Applied Superconductivity*, 24(3):1–4, 2014.

[6] T Rummel, K Risse, Johann Kisslinger, M Köppen, F Fullenbach, George Hutch Neilson, Thomas Brown, and S Ramakrishnan. The Trim Coils for the Wendelstein 7-X Magnet System. *IEEE Transactions on Applied Superconductivity*, 22(3):4201704–4201704, 2012.

[7] Tomohiro Morisaki, Mamoru Shoji, Suguru Masuzaki, Satoru Sakakibara, Hiroshi Yamada, Akio Komori, and Osamu Motojima. Flux Surface Mapping in LHD. *Fusion Science and Technology*, 58(1):465–470, 2010.

[8] Peter Drewelow, Torsten Bräuer, Matthias Otte, Friedrich Wagner, and Andreas Werner. Three-dimensional photogrammetric measurement of magnetic field lines in the WEGA stellarator. *Review of Scientific Instruments*, 80(12):123501, 2009.

[9] J T Peterson, G J Hartwell, S F Knowlton, J Hanson, R F Kelly, and C Montgomery. Initial Vacuum Magnetic Field Mapping in the Compact Toroidal Hybrid. *Journal of Fusion Energy*, 26(1-2):145–148, December 2006.

[10] M Otte and et al. Setup and initial results from the magnetic flux surface diagnostics at wendelstein 7-x. *Plasma Physics and Controlled Fusion*, XX(XX):XX2016, January 2016.

[11] Sergey A Bozhenkov, Joachim Geiger, M Grahl, Johann Kisslinger, A Werner, and R C Wolf. Fusion Engineering and Design. *Fusion Engineering and Design*, 88(11):2997–3006, November 2013.

[12] Doug McCune. Pspline – princeton spline and hermite cubic interpolation routines. Online. http://w3.pppl.gov/ntcc/PSPLINE/.

[13] James D Hanson and Steven P Hirshman. Compact expressions for the Biot–Savart fields of a filamentary segment. *Physics of Plasmas*, 9(10):4410, 2002.

[14] The Numerical Algorithms Group (NAG). The nag library. Oxford, United Kingdom www.nag.com.

[15] A C Hindmarsh. ODEPACK, A Systematized Collection of ODE Solvers, RS Stepleman et al.(eds.), North-Holland, Amsterdam,(vol. 1 of), pp. 55-64. *IMACS transactions on scientific computation*, 1983.

[16] D Sarafyan. Improved Sixth-Order Runge-Kutta Formulas and Approximate Continuous Solution of Ordinary Differential Equations. *Journal of Mathematical Analysis and Applications*, 40(2):436–&, 1972.

[17] Stuart R Hudson and Yasuhiro Suzuki. Chaotic coordinates for the Large Helical Device. *Physics of Plasmas*, 21(10):102505, October 2014.

[18] Allen H Boozer. Physics of magnetically confined plasmas. *Rev.Mod.Phys.*, 76:1071–1141, 2004.